ACS NANO

www.acsnano.org

ARTICLE

Urease-Powered Micromotors with Spatially Selective Distribution of Enzymes for Capturing and Sensing Exosomes

Xiaoxia Liu, Yong Wang, Yixin Peng, Jinjin Shi, Wenjun Chen,* Wei Wang,* and Xing Ma*

Cite This: *ACS Nano* 2023, 17, 24343−24354

Read Online

ACCESS | Metrics & More | Article Recommendations | Supporting Information

ABSTRACT: Enzyme-catalyzed micro/nanomotors (MNMs) exhibit tremendous potential for biological isolation and sensing, because of their biocompatibility, versatility, and ready access to biofuel. However, flow field generated by enzyme-catalyzed reactions might significantly hinder performance of surface-linked functional moieties, e.g., the binding interaction between MNMs and target cargos. Herein, we develop enzymatic micromotors with spatially selective distribution of urease to enable the independent operation of various modules and facilitate the capture and sensing of exosomes. When urease is modified into the motors' cavity, the flow field from enzyme catalysis has little effect on the exterior surface of the motors. The active motion and encapsulating urease internally result in enhancement of ∼35% and 18% in binding efficiency of target cargos, e.g., exosomes as an example here, compared to their static counterparts and moving micromotors with urease modified externally, respectively. Once exosomes are trapped, they can be transferred to a clean environment by the motors for Raman signal detection and/or identification using the surface Raman enhancement scattering (SERS) effect of coated gold nanoshell. The biocatalytic micromotors, achieving spatial separation between driving module and function module, offer considerable promise for future design of multifunctional MNMs in biomedicine and diagnostics.

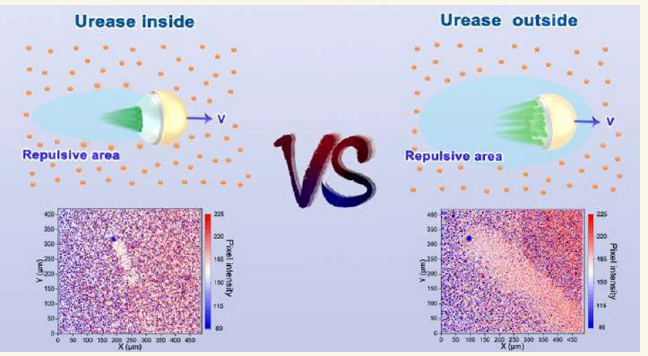

KEYWORDS: *enzymatic micromotors, spatially distribution, flow field, driving module, functional module*

INTRODUCTION

Chemically driven micro/nanomotors (MNMs) are synthetic micro/nanomachines that convert chemical energy into mechanical energy, enabling them to self-propel and perform specific tasks.[1,2] In particular, enzymes acting as a special catalytic engine can complete the energy conversion through enzyme-catalyzed reactions. There are plenty of benefits by using enzymes as the catalysts to power MNMs, such as the biocompatibility, fuel bioavailability, and high turnover rates.[3,4] In order to promote the development of enzyme-driven MNMs, more and more enzymes, such as catalase,[5,6] urease,[7,8] glucose oxidase,[9,10] and lipase[11,12] have been decorated on mesoporous silica, polymer, metal−organic frameworks, and cells, achieving the desired MNMs.

In the realm of enzyme-driven MNMs, enzymes play a crucial role as the propulsion engine responsible for converting energy and facilitating the motor's self-propulsion. Simultaneously, to unlock their full potential for practical applications, these enzyme-driven MNMs necessitate multifaceted module designs that seamlessly merge mobility with additional functionalities including sensing and recognition capabilities. By virtue of the autonomous motion, enzyme-powered MNMs can achieve on-the-fly capture or binding of target substances by modifying specific ligands such as aptamers or antibodies. For example, Sánchez et al. developed enzyme-powered nanomotors modified with urease and antibodies for active targeting of bladder cancer cells.[13] Li et al. decorated catalase and aptamers on the electrospinning fibers to construct micromotors for rapid capture of circulating tumor cells.[14] These reported MNMs contain two components simultaneously: one is the engine part (enzyme) and the other is the functional part (antibody or aptamer). However, there is no

Received: October 23, 2023
Revised: November 21, 2023
Accepted: November 28, 2023
Published: December 1, 2023

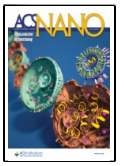

https://doi.org/10.1021/acsnano.3c10405
ACS Nano 2023, 17, 24343−24354

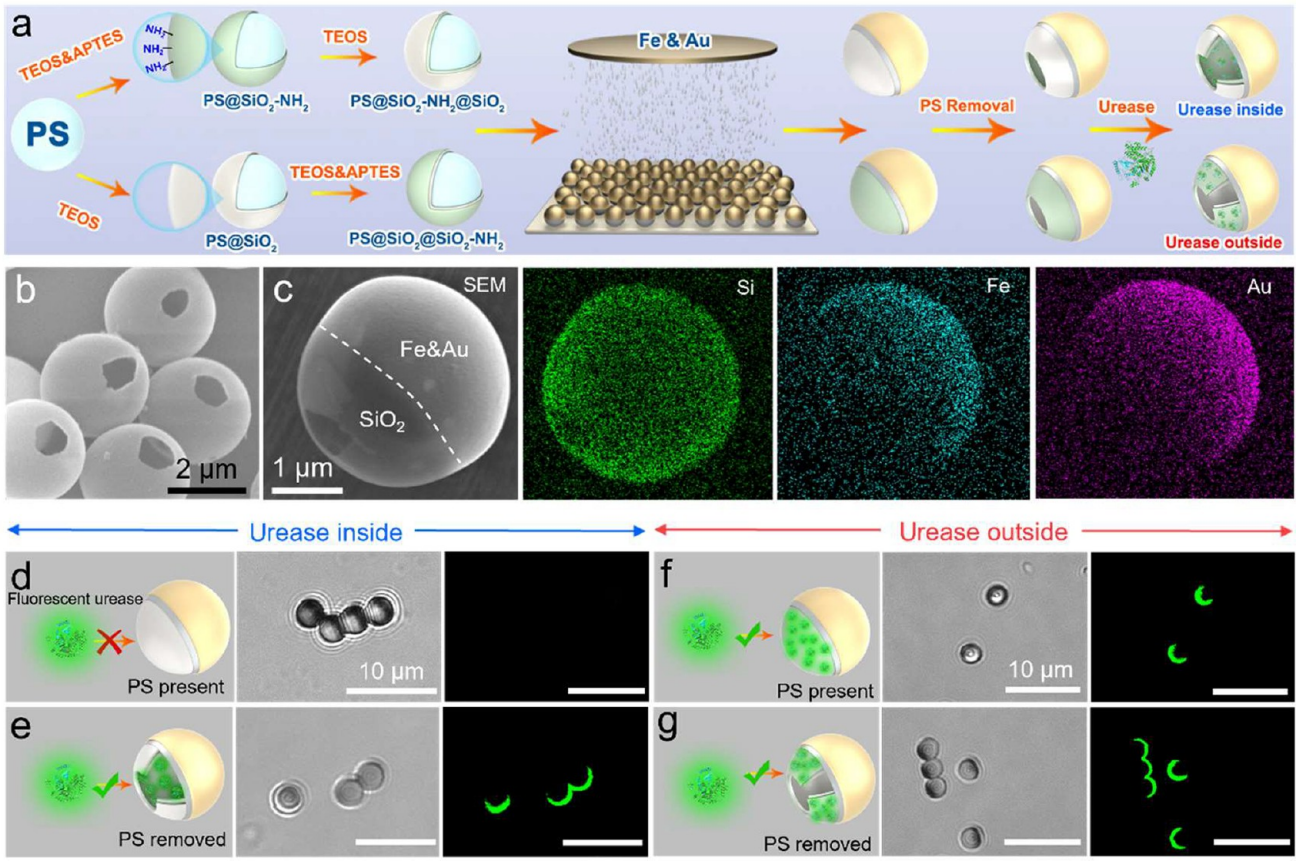

Figure 1. Preparation and characterization of $HSiO_2FA$-Urease-I (Urease inside) and $HSiO_2FA$-Urease-O (Urease outside) micromotors. (a) Schematic diagram depicting the experimental process employed to fabricate $HSiO_2FA$-Urease-I and $HSiO_2FA$-Urease-O micromotors. (b, c) SEM image and EDX mapping of $HSiO_2FA$ microparticles. (d–g) Bright-field and fluorescent images of PSSFA-NH_2–I (panel (d)), $HSiO_2FA$-NH_2–I (panel (e)), PSSFA-NH_2–O (panel (f)), and $HSiO_2FA$-NH_2–O (panel (g)) modified with FITC-urease.

discernible space between the functional component and the engine component. In this case, the flow field generated by the enzyme-catalyzed reaction might influence the binding interaction between the target and the aptamer (or antibody) due to inherently spatial conflict. Segregating the driving module from the functional module mitigates the likelihood of mutual interference. At the micro/nanoscale, such interference can have detrimental effects, potentially resulting in performance deterioration or mission failure. Accordingly, in order to guarantee effective operation, it is crucial to distribute the function module and the engine module in different compartments of the MNMs.

Exosomes are liquid/protein vesicles characterized by a double-membrane structure with a diameter ranging from 50 to 150 nm. They originate from late endosomes in the intracellular endocytic system, and they are present in multiple body fluids, including blood, saliva, urine, and cerebrospinal fluid. As a result of being rich in proteins, mRNA, DNA, and lipids, exosomes can provide the unique information on diseases, serving as the noninvasive cancer biomarkers for clinical diagnosis.[15,16] Meanwhile, the isolation and enrichment of exosomes is a pivotal issue for their further studies and applications.[17] To date, numerous techniques, such as ultracentrifugation,[18] size exclusion chromatography,[19] density gradient separation,[20] and polymer-based precipitation,[21] have been developed to isolate exosomes, each with its own advantages and disadvantages, in terms of the purity and sample recovery. Recently, another method which relies on the binding between the aptamer (or antibody) and the surface protein (CD9, CD63, CD81) of exosomes also has been employed to isolate exosomes.[22−24] However, the binding between the aptamer (or antibody) and the surface proteins of exosomes is usually completed by passive diffusion in solution, which leads to low capturing efficiency. Moreover, current techniques still lack controllability and in situ sensing capability on the captured exosome at a small scale. Recently, Guan et al. fabricated micromotors with axis-asymmetric bowl-shaped structure to enhance mass transfer[25] and molecule enrichment[26] through spontaneous multipattern motion. Thus, we anticipate that exploiting the motion characteristics of MNMs can offer a promising avenue for exosome isolation and detection.

To enable efficient separation and downstream analysis of exosomes using enzyme-driven MNMs, in this work, we demonstrated urease-powered micromotors with controlled enzyme distribution achieved through selective modification of the amino group. The as-prepared micromotors consist of hollow multilayered SiO_2 ($HSiO_2$)@Fe@Au ($HSiO_2FA$), with ureases immobilized on the inner surface. The urease-decorated micromotors can be propelled by a urease-catalyzed urea decomposition reaction. Compared with the micromotor modified by urease outside, when the enzyme is modified to the inner surface, the flow field generated has much less influence on the external surface of the motors. In view of this phenomenon, urease was coupled on the inside of hollow SiO_2 to induce movement in the presence of urea, while DNA

https://doi.org/10.1021/acsnano.3c10405
ACS Nano 2023, 17, 24343−24354

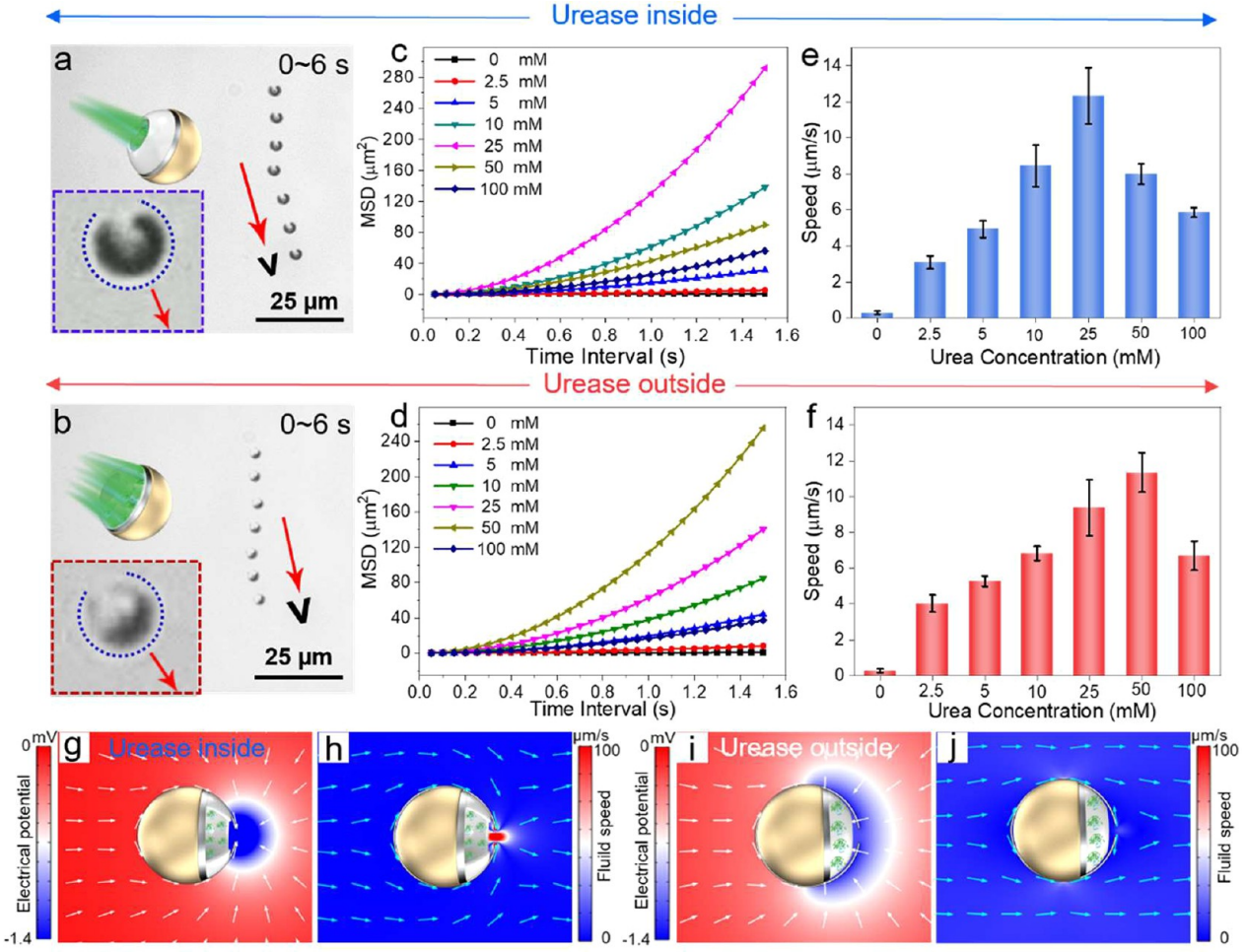

Figure 2. Motion behaviors of the $HSiO_2FA$-Urease-I and $HSiO_2FA$-Urease-O micromotors. (a, b) Superimposed image of sequential frames of a typical $HSiO_2FA$-Urease-I and $HSiO_2FA$-Urease-O micromotor swimming in urea solution and the inset is a magnified image of the two micromotor suggesting their moving direction is against the hole. (c, d) Mean-square-displacement (MSD) versus the time interval (Δt) of $HSiO_2FA$-Urease-I (panel (c)) and $HSiO_2FA$-Urease-O (panel (d)) micromotors in varied urea concentrations. (e, f) Speed of $HSiO_2FA$-Urease-I (panel (e)) and $HSiO_2FA$-Urease-O (panel (f)) micromotors moving in urea solution with different concentrations. (g– j) Numerical simulations of the electric potential and the fluid field around a typical $HSiO_2FA$-Urease-I (panels (g) and (h)) and $HSiO_2FA$-Urease-O (panels (i) and (j)) micromotor. Error bars indicate the standard deviation (N = 10).

aptamers that can target exosomes were attached on the outside via Au−S bond, thus reducing the influence of the proton flow on target binding. In addition, the motion of internal urease modified micromotors can increase the binding probability of the aptamer and the specific surface protein about exosomes, resulting in rapid capture of exosomes. Furthermore, the micromotors serve as active SERS probes for the analysis for trapped exosomes by utilizing the coated Au and Fe nanoshell. Such self-propelled urease micromotors that separate the functional and driving modules hold considerable promise for future rational design of biomedical MNMs, especially in the applications of biochemical sensing and biomedical diagnosis.

RESULTS AND DISCUSSION

Preparation and Characterization of Urease Internally and Externally Modified Hollow SiO_2 Micromotors. The polystyrene encapsulated with silica (PS@SiO_2) microparticles were fabricated by a two-step co-condensation method using polystyrene (PS) microparticles as the templates (Figure 1a), following our previously reported strategy.[27] The scanning electron microscopy (SEM) images of PS and PS@SiO_2 in Figures S1a and S1b in the Supporting Information show an average diameter of 3.0 ± 0.2 μm. Because the layer of silica is only ∼28 nm (Figure S2) in the Supporting Information, there is no significant difference between the sizes of PS and PS@SiO_2. Subsequently, a thin layer of Fe (10 nm) and Au (10 nm) were sputtered on the monolayered PS@SiO_2 microparticles to form PS@SiO_2@Fe@Au (PSSFA), which can be clearly observed from the SEM image in Figure S1c in the Supporting Information. Besides, the highly concentrated PS templates tend to cluster together, resulting in SiO_2 growth only on their exposed surfaces.[27,28] As a result, when the PS templates were removed, the SEM image of the obtained hollow SiO_2@Fe@Au ($HSiO_2FA$) showed that there was a hole with a diameter of 767 ± 98 nm on the hollow particle (Figure 1b), which provides the route for urease molecules (∼11 nm × 6 nm) to enter the cavity.[29] The corresponding elemental analysis with energy-dispersive X-ray (EDX) spectroscopy demonstrated that the Fe and Au layers were on opposite hemispheres of the hole of $HSiO_2FA$, where the bilayers endowed the microparticles with properties of magnetism and functionalization (Figure 1c).

https://doi.org/10.1021/acsnano.3c10405
ACS Nano 2023, 17, 24343−24354

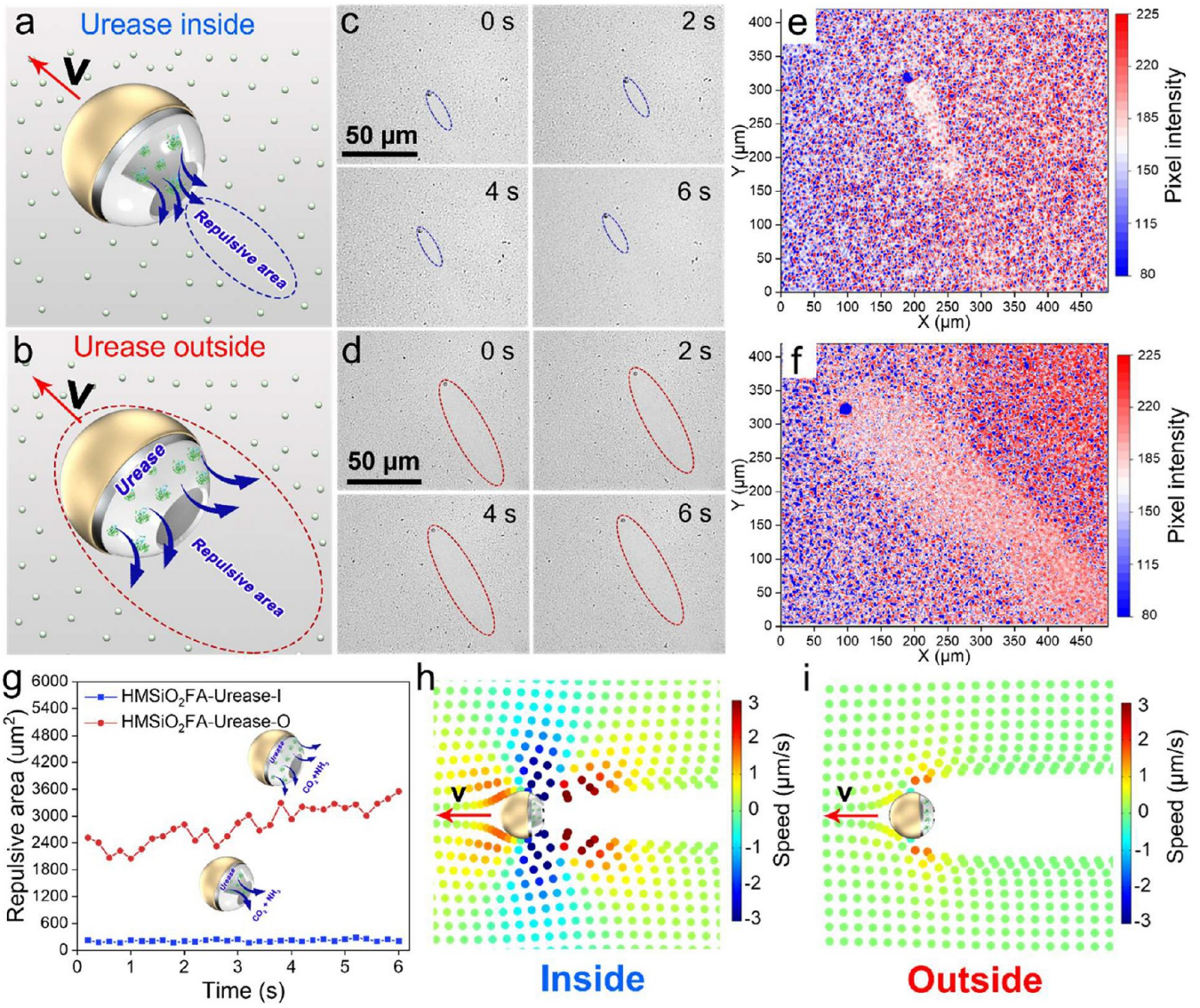

Figure 3. Influence on surrounding of flow field generated from the $HSiO_2FA$-Urease-I and $HSiO_2FA$-Urease-O micromotors. (a, b) Scheme illustrating the impact of a $HSiO_2FA$-Urease-I (panel (a)) and $HSiO_2FA$-Urease-O (panel (b)) micromotor on the surrounding tracer particles during their motion. (c, d) Time-lapse images of a typical $HSiO_2FA$-Urease-I micromotor (panel (c)) and a $HSiO_2FA$-Urease-O micromotor (panel (d)) moving in 25 and 50 mM urea solution containing tracer particles, respectively. (e, f) Density maps of the $HSiO_2FA$-Urease-I micromotors (panel (e)) and $HSiO_2FA$-Urease-O micromotors (panel (f)) obtained by calculating the pixel intensity at t = 6 s of the videos. (g) Statistical plots of the repulsion area of the surrounding particles by the $HSiO_2FA$-Urease-I and $HSiO_2FA$-Urease-O micromotors at different times. (h, i) Simulation showing the impact of flow field from the $HSiO_2FA$-Urease-I micromotors (panel (h)) and $HSiO_2FA$-Urease-O micromotors (panel (i)) on surrounding particles.

Given that $HSiO_2FA$ has a hollow structure with a hole, we can selectively decorate the interior or exterior surface with urease through selective modification of the amino group. Figure 1a shows the schematic illustration of the fabrication process, while further details are provided in the Materials and Methods. To prepare the urease modified inside of $HSiO_2FA$ ($HSiO_2FA$-Urease-I), first, a silica layer with amino group embedded inside was formed on the surface of PS microparticles ($PS@SiO_2-NH_2$) via a co-condensation method. Then, another layer of bare silica was further grown on top to shield the amino group existing outside the $PS@SiO_2-NH_2$, to obtain amine ($-NH_2$)-modified inside $PS@SiO_2$ ($PS@SiO_2-NH_2@SiO_2$) microparticles. The zeta potential values of PS (-0.17 ± 0.02 mV) and $PS@SiO_2-NH_2$ (30.8 ± 0.8 mV) in Figure S3a in the Supporting Information confirmed the successful coating of silica on PS microparticles and the functionalization of amino groups. Meanwhile, the zeta potential of $PS@SiO_2-NH_2@SiO_2$ was -3.6 ± 0.3 mV, which also proved that the outside amino groups were shielded as planned. Then, a thin layer of Fe (10 nm) and Au (10 nm) was sputtered on $PS@SiO_2-NH_2@SiO_2$ microparticles to form $PS@SiO_2-NH_2@SiO_2@Fe@Au$ ($PSSFA-NH_2-I$). After the removal of PS, the zeta potential of the microparticles changed from -4.2 ± 1.0 mV to 9.9 ± 2.7 mV, showing the exposure of the internal amino groups. To further detect the amide groups of $HSiO_2FA-NH_2-I$, we also used fluorescamine to react with the amine groups and emit fluorescence at 477 nm. The difference of fluorescent intensity at 477 nm of the two samples in Figure S3b in the Supporting Information proved that the removal of the PS template revealed the

https://doi.org/10.1021/acsnano.3c10405
ACS Nano 2023, 17, 24343−24354

internal amino groups. The result is consistent with the zeta potential measurement. Furthermore, by comparing the fluorescence images of PSSFA-NH_2−I as a control and $HSiO_2$FA-NH_2−I modified with FITC-urease under the same condition, it was found that the PS-removed sample ($HSiO_2$FA-NH_2−I) exhibited green fluorescence, which is from the FITC-urease (Figure 1e), while the PSSFA-NH_2−I showed no obvious fluorescence signal (Figure 1d). The results verified the successful immobilization of urease on the inner surface of $HSiO_2$FA-NH_2−I microparticles exclusively ($HSiO_2$FA-Urease-I). Similarly, we selectively functionalized the amino groups, then urease on the exterior of the particles to form the external urease modified hollow SiO_2 ($HSiO_2$) @ Fe@Au ($HSiO_2$FA-Urease-O), which was proved by zeta potential (Figure S4a in the Supporting Information), fluorescence spectrum (Figure S4b in the Supporting Information) and fluorescence images (Figures 1f and 1g).

Motion Behaviors of the $HSiO_2$FA-Urease-I and $HSiO_2$FA-Urease-O Micromotors. The urease immobilized on the micromotors ($HSiO_2$FA-Urease-I and $HSiO_2$FA-Urease-O) can catalyze the decomposition of urea into NH_3 and CO_2, propelling the motion of the micromotors. The typical video snapshots of $HSiO_2$FA-Urease-I and $HSiO_2$FA-Urease-O micromotor moving in 25 mM urea solution are shown in Figures 2a and 2b. It can be observed that both $HSiO_2$FA-Urease-I and $HSiO_2$FA-Urease-O micromotors performed active motion and were moving away from the hole on the micromotors (see the inset images in Figures 2a and 2b). The typical videos of $HSiO_2$FA-Urease-I and $HSiO_2$FA-Urease-O micromotors in urea solution of different concentrations (0, 2.5, 5, 10, 25, 50, 100 mM) are provided in Videos S1 and S2 in the Supporting Information. Based on the extracted 2D coordinates (x, y) along the trajectories, the curves of mean square displacement (MSD) versus the time interval (Δt) in different urea concentrations are shown in Figures 2c and 2d. As the fuel concentration increased, the MSD curves of $HSiO_2$FA-Urease-I and $HSiO_2$FA-Urease-O micromotors exhibited a more parabolic shape, suggesting a shift from diffusive to ballistic motion. The slopes in the linear range of the curves increased until the urea concentration reached 25 mM for $HSiO_2$FA-Urease-I and 50 mM for $HSiO_2$FA-Urease-O micromotors, which was also consistent with the speed results obtained by measuring the length of the particle trajectory within a defined time period in Figures 2e and 2f. The observed reduction in micromotors' speed at high urea concentrations is due to the inhibition of enzymatic activity that commonly happens at elevated substrate concentrations.[30]

In order to understand the propulsion mechanism of the micromotors, we performed numerical modeling of a $HSiO_2$FA-Urease-I and $HSiO_2$FA-Urease-O micromotor (Figure S5 in the Supporting Information; modeling details are presented in the Materials and Methods). The ureases of the micromotors ($HSiO_2$FA-Urease-I and $HSiO_2$FA-Urease-O) decomposed the urea into CO_2 and NH_3, which subsequently converted to ionic products such as NH_4^+, HCO_3^-, CO_3^{2-}, and OH^- in aqueous solution. Since the reaction between HCO_3^- and OH^- would produce CO_3^{2-} and H_2O, at a solution pH of 9, the dominant species present are CO_3^{2-} and NH_4^+.[31] We made an assumption that there was a uniform outward flux of NH_4^+ and CO_3^{2-} ions from the micromotors, disregarding the effect of OH^- and HCO_3^-. The diffusion rate of NH_4^+ is faster than that of CO_3^{2-} (1.95×10^{-9} vs 0.92×10^{-9} m^2/s),[32] an electric field pointing from the Au hemisphere toward the hole was formed spontaneously to maintain electroneutrality outside the electrical double layers. (See Figures 2g and 2i.) The electric field induced a slip velocity pointing in the same direction in the electric double layer of the negatively charged micromotors (Figures 2h and 2j). It is this slip flow that causes the micromotors to move away from the hole-existing side, which is in accordance with the experimental results (insets of Figures 2a and 2b). Nevertheless, our model just provided a possible explanation of the moving direction of the Janus enzyme-powered microrobots by an ionic self-diffusiophoresis mechanism.[33]

Influence of Flow Field Generated by the $HSiO_2$FA-Urease-I and $HSiO_2$FA-Urease-O Micromotors in Their Vicinity. To test the impact of the flow field generated by the $HSiO_2$FA-Urease-I and $HSiO_2$FA-Urease-O micromotors on their vicinity, SiO_2 nanoparticles were employed as tracer particles to visualize the affected region. The motion of the $HSiO_2$FA-Urease-I and $HSiO_2$FA-Urease-O micromotors was controlled at the same speed. Therefore, the urea concentrations in solution are 25 mM for $HSiO_2$FA-Urease-I micromotors and 50 mM for $HSiO_2$FA-Urease-O micromotors, respectively. Figures 3c and 3d demonstrate that the repulsive area generated by $HSiO_2$FA-Urease-I and $HSiO_2$FA-Urease-O micromotors remained largely unchanged throughout their motion. The corresponding videos are presented in Video S3 in the Supporting Information. To quantitatively compare the influence of the flow field produced by these two micromotors on the surrounding particles, we calculated the repulsive area around the SiO_2 nanoparticles at different times. As illustrated in Figure 3g, we observed that the $HSiO_2$FA-Urease-I micromotors (~209 μm^2) had a smaller impact on the surrounding substances and a smaller repulsive area on nanoparticles, compared to those of the $HSiO_2$FA-Urease-O micromotors (~2803 μm^2). The influenced range of the flow field generated by $HSiO_2$FA-Urease-I micromotors was only 7% of that exhibited by $HSiO_2$FA-Urease-O micromotors. In order to enhance our understanding of influence on surrounding particles from the $HSiO_2$FA-Urease-I and $HSiO_2$FA-Urease-O micromotors, we created density maps that involved the pixel intensity values of video frames at $t = 6$ s using a color map. When the $HSiO_2$FA-Urease-I micromotor migrated away from the hole, it can be seen clearly that only the SiO_2 nanoparticles located at its opening were repelled (Figures 3e and 3a). However, in the case of the $HSiO_2$FA-Urease-O micromotors, Figures 3f and 3b revealed that a significant proportion of the surrounding SiO_2 particles were repelled.

In addition, we conducted simulations to investigate the impact of the two micromotors on the surrounding particles. The results, depicted in Figures 3h and 3i, revealed that the $HSiO_2$FA-Urease-I micromotor exhibited a smaller repulsive area than the $HSiO_2$FA-Urease-O micromotor. Notably, our simulation results align with the observations made in our experiment. The phenomenon can be explained by the distinct spatial distribution of enzymes. Specifically, when urease is modified inside the micromotor, the catalytic process takes place within the cavity, resulting in the accumulation of a substantial amount of catalytic products in the cavity. As a result, the generated electric field is primarily concentrated in the cavity, and as the motor moves, the flow field has a minimal effect on the surrounding substances. On the contrary, when the urease is modified on external surface of micromotors, the

https://doi.org/10.1021/acsnano.3c10405
ACS Nano 2023, 17, 24343−24354

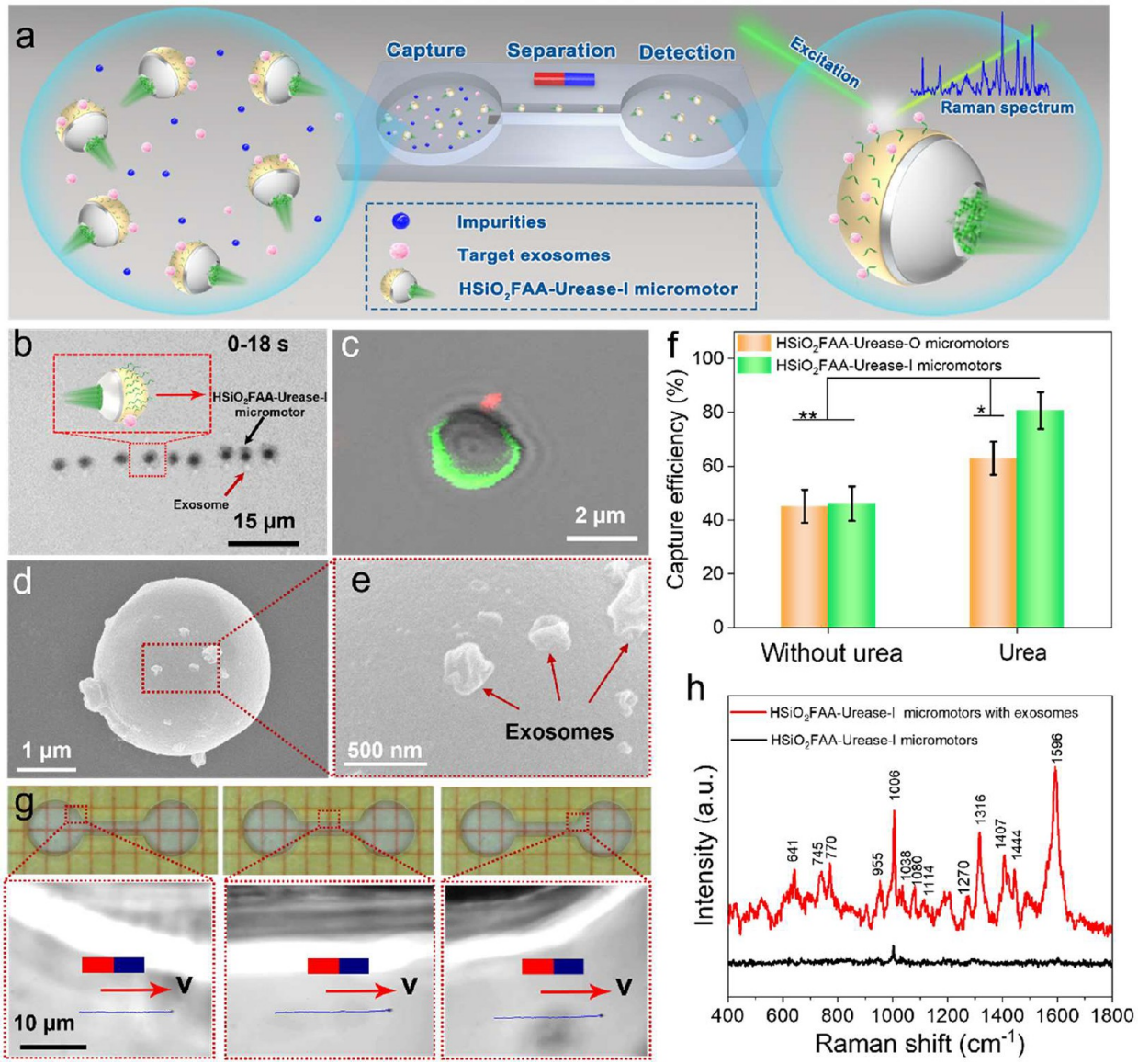

Figure 4. Capture and detection of exosomes in a channel using aptamer-modified $HSiO_2$FA-Urease-I micromotors. (a) Schematic diagram depicting the process employing aptamer-modified $HSiO_2$FA-Urease-I micromotor to capture and transport the exosomes from a raw sample to a clean well for detection applications. (b) Superimposed image of sequential frames of a $HSiO_2$FAA-Urease-I micromotor with exosome swimming in 25 mM urea solution. (c–e) Fluorescence image (panel (c)) and SEM images (panels (d) and (e)) of the $HSiO_2$FAA-Urease-I micromotor capturing exosomes on the surface. (f) The capture efficiency of exosomes using the $HSiO_2$FAA-Urease-I and $HSiO_2$FAA-Urease-O micromotors under different conditions. Error bars indicate standard deviation (N = 3). (g) Video snapshots of the movement of the $HSiO_2$FAA-Urease-I micromotor transporting exosome guided by a magnetic field. (h) SERS spectra of exosomes captured by $HSiO_2$FAA-Urease-I micromotor.

catalytic process occurs on the surface of the motor, resulting in the dispersion of the electric and flow fields across the surface. This distribution of flow fields affects a broader range of the surrounding particles. Overall, the location of the modified enzyme plays a critical role in determining the distribution of the generated flow fields, which, in turn, affects the behavior of the micromotors and their surrounding environment.

Exosomes Capture and Detection Using $HSiO_2$FA-Urease-I Micromotors. Given that the flow field generated by the $HSiO_2$FA-Urease-I micromotor exhibits a limited effect on excluding the surrounding particles, DNA aptamers that can target exosomes were modified to their surface through Au–S bonds, resulting in the creation of aptamer-linked micromotors called $HSiO_2$FAA-Urease-I. The corresponding change in zeta potential for $HSiO_2$FA-Urease-I (−10.9 ± 1.1 mV) and $HSiO_2$FAA-Urease-I (−19.1 ± 2.7 mV) confirmed the successful aptamer surface modification of the micromotors. With the aptamer-modified micromotors successfully constructed, we proceeded to use them for the capture and detection of exosomes.

As illustrated in Figures 4a and 4g, we designed a chip consisting of two chambers (capture and detection wells) connected by a channel. A typical experiment showing the exosomes being captured by a $HSiO_2$FAA-Urease-I micromotor in the capture well is shown in Video S4 in the Supporting Information. The corresponding optical images are shown in Figure S6 in the Supporting Information. In a

https://doi.org/10.1021/acsnano.3c10405
ACS Nano 2023, 17, 24343–24354

solution containing urea, the $HSiO_2$FAA-Urease-I micromotor initially exhibited random movement around the exosome. At t = 1 s, the $HSiO_2$FAA-Urease-I micromotor successfully targeted and bonded to the exosome due to the presence of aptamers. After the exosomes were trapped, the $HSiO_2$FAA-Urease-I micromotors continued to move in the urea solution while carrying the exosomes (see Figure 4b and Video S5). The fluorescence image confirmed that the red fluorescent exosome was successfully conjugated onto the gold coating surface of the micromotor (Figure 4c). Furthermore, Figure 4d and 4e show that after exosomes were captured, spherical vesicles were clearly found on the surface of the micromotor, and each micromotor was capable of capturing multiple exosomes. The concentration of exosomes in the capture well significantly decreased after the capture process, and nanoparticle tracking analysis (NTA) system was used to measure the concentration of exosomes before and after capture. Exosome capture by using the $HSiO_2$FAA-Urease-I micromotors at various urea concentrations was tested. As depicted in Figure S7 in the Supporting Information, the highest exosome capture efficiency was achieved at a urea concentration of 25 mM, which is attributed to the micromotors' enhanced movement speed at this concentration. In addition, the nonspecific adsorption of the $HSiO_2$FA-Urease-I micromotors was also was investigated. This result showed that the nonspecific adsorption of exosomes by the $HSiO_2$FA-Urease-I micromotors was negligible. (See Figure S8 in the Supporting Information.) To facilitate a comprehensive comparison of exosome capture by the $HSiO_2$FAA-Urease-I and $HSiO_2$FAA-Urease-O micromotors, we selected the optimal urea concentration for each micromotors' movement. The NTA test results are shown in Figure S9 in the Supporting Information. The results indicated that the isolation efficiency of $HSiO_2$FAA-Urease-I micromotors in the presence of urea (25 mM) was ~80.7%, which was superior to that of the $HSiO_2$FAA-Urease-O micromotor with 50 mM urea (63%) and the $HSiO_2$FAA-Urease-I micromotor without urea (46.1%). (Figure 4f). There are two main reasons that could potentially explain the significant enhancement in the capturing efficiency. First, the contact between the aptamer on the passive micromotors and the exosomes in solution is limited. However, the micromotors' movement can increase the probability of contact with exosomes, thereby improving their capture efficiency. Second, the catalytic reaction occurs within the cavity during the process of urease-powered $HSiO_2$FAA-Urease-I micromotors, while the flow field generated by the micromotors is primarily focused on the hole. As a result, the impact of the flow field on the bond between the micromotors and exosomes would be minimized.

Subsequently, using a magnetic field, the specific $HSiO_2$FAA-Urease-I micromotor that captured the exosomes was directed through the channel to the detection well (see Figure 4g, as well as Video S6 in the Supporting Information). SERS technology is a promising tool for biosensing, offering rapid detection and fingerprint identification capabilities for unknown analytes with ultralow concentration.[34] Here, once $HSiO_2$FAA-Urease-I micromotors trapping with exosomes reached the detection well, we utilized the SERS effect of the coated Au film to detect the Raman signals of the exosomes. The Raman spectra obtained from exosomes between peaks and assignments are shown in Table S1 in the Supporting Information. As shown in Figure 4h, the major peaks appearing in the Raman spectra were located at 641 cm^{-1} (tyrosine), 745 cm^{-1} (symmetric breathing of tryptophan), 770 cm^{-1} (nucleic acid), 955 cm^{-1} (lipids), 1006 cm^{-1} (phenylalanine, symmetric stretching of the phosphodioxy moiety), ~1038 cm^{-1} (proline), 1080 cm^{-1} (nucleic acid, lipid), 1114 cm^{-1} (phenylalanine), 1270 cm^{-1} (cytosine), ~1316 cm^{-1} (phospholipids), 1407 cm^{-1} (C═O symmetric stretch), 1444 cm^{-1} (CH_2 and CH_3 deformation vibrations, cholesterol, fatty acid band), and 1596 cm^{-1} (G about DNA/RNA, CH deformation about proteins and carbohydrates).[35−37] These peaks are mainly associated with lipids, amino acids, proteins, and nucleic acids, which are the primary components of exosomes.[37] Their characteristic Raman spectra provides a powerful tool for identifying and quantifying exosomes in biological samples. Compared to the previously reported exosome capture methods, the enzymatic micromotors active platform demonstrates comparable capture efficiency, while their motion significantly reduces the operating time (Table S2 in the Supporting Information). Furthermore, this enzyme-driven micromotor-based platform fully exploits the advantages of its motion to capture exosomes and combines it with Raman detection, achieving the integration of exosome capture and detection. Consequently, the enzyme-driven micromotor-based platform holds practical application potential in disease diagnosis and prognosis.

To explore the application potential of the $HSiO_2$FAA-Urease-I micromotor in a complex matrix, the enzyme activity of the $HSiO_2$FAA-Urease-I micromotor was measured in real plasma and urine. As shown in Figure S10 in the Supporting Information, plasma and urine did not affect the urease activity, confirming their stability in real samples. In the capture well of a chip, exosomes are captured from the plasma and urine after collection and preprocessing. As demonstrated in Figures S11 and S12, as well as Video S7 in the Supporting Information, the $HSiO_2$FAA-Urease-I micromotor exhibited long-range motion in pretreated plasma (4.68 ± 0.99 μm/s) and urine (5.35 ± 1.09 μm/s), indicating the practical usefulness of these motors in realistic scenarios. Moreover, in the complex matrix, exosomes can be trapped on the surface of the $HSiO_2$FAA-Urease-I micromotor. (See Figure S13 in the Supporting Information.) The exosomes capture efficiency in the complex matrix (Figure S14 in the Supporting Information) showed that, even though the complex matrix would influence the capture efficiency, $HSiO_2$FAA-Urease-I micromotors exhibited enhanced capture efficiency due to their mobility and enzyme's internal modification, which was consistent with the results in Figure 4f. The $HSiO_2$FAA-Urease-I micromotors with exosomes were transferred to the clean detection well for Raman analysis under magnetic fields, and the results are shown in Figure S15 in the Supporting Information. The peaks in Raman spectra are associated with phospholipids, proteins, and nucleic acids present in the extracellular vesicles. All of these findings confirmed the potential application of these $HSiO_2$FAA-Urease-I micromotors in clinical samples in the future. Furthermore, SERS biosensors can offer the potential of the simultaneous analysis of multiple components in a complex mixture, achieved by using different types of nanoparticles or substrates that generate unique Raman spectra for each target molecule. Therefore, in the future, different SERS probes decorated with different Raman reporters and specific aptamer for targeting specific exosomes can be designed. Combined with the enzyme-driven micromotor active platform and SERS probes, it is expected to realize the simultaneous detection of

https://doi.org/10.1021/acsnano.3c10405
ACS Nano 2023, 17, 24343−24354

multiple types of exosomes, thereby advancing the feasibility of clinical cancer screening.

CONCLUSIONS

In conclusion, we have developed urease-powered micromotors with selective distribution of the enzyme to capture and detect exosomes. To achieve controlled enzyme distribution, amino groups were selectively modified onto the inner or outer surface of hollow silica by a two-step co-condensation method. The spatial distribution of urease was confirmed by a variety of characterization methods, including fluorescence images, zeta potential, and fluorescence spectra. The micromotors with ureases immobilized on either the inner or outer surface demonstrated an excellent motion performance. Through experimental study and numerical simulations, it was found that $HSiO_2$FA-Urease-I micromotor, with an enzyme-catalyzed reaction occurring within its cavity, exhibits a significant reduction of ∼93% in the influence area generated by its flow field, compared to $HSiO_2$FA-Urease-O micromotor, which contributes the efficient realization of the function on the outer surface of the $HSiO_2$FA-Urease-I micromotor. In addition, we further took full advantage of the $HSiO_2$FA-Urease-I micromotors' movement and functionalization to capture−transport−detect exosomes. The spatial separation between the driving module and the functional module of micromotors promoted the targeting of specific substances and the effective realization of on-demand functionalities.

Taken together, controlled spatial distribution of enzymes on a urease micromotor deepens our understanding of the fundamental principles underlying enzyme-driven MNMs, and could facilitate the development of more-rational designs to ensure their practical application in the near future. Despite existing limitations, efforts will be made to enhance ion tolerance of $HSiO_2$FA-Urease-I micromotors by incorporating customized surface functionalities (polyelectrolyte coating[38]), as well as exploring morphological and structural properties (porous structure[39]). Furthermore, the modification of distinct functional ligands on the outer surface will enable the $HSiO_2$FA-Urease-I micromotors to identify and sort different biomarkers in both real biological samples and organisms.

MATERIALS AND METHODS

Materials and Characterization. Poly(vinylpyrrolidone) (K-30, >98%), styrene, 2,2′-azo-bis(isobutyronitrile) (AIBN, 98%), isopropanol (IPA), cetyltrimethylammonoium bromide (CTAB, 99%), ammonia ($NH_3{\cdot}H_2O$, 25%), tetraethylorthosilicate (TEOS, 99%), 3-aminopropyltriethoxysilane (APTES, 99%), ethanol (EtOH, >99%), dimethylformamide (DMF, >99%), glutaraldehyde (50%), Jack bean urease (Type IX, powder, 50 000−100 000 unites g^{-1} solid), tris(2-carboxyethyl) phosphine hydrochloride (TCEP), and 6-mercaptohexanol (MCH) were purchased commercially and used as-received. SEM images and EDX spectroscopy analyses were made (Carl Zeiss GmbH Gemini SEM 300 microscope and Oxford Instruments X-Max system, respectively. An electron beam (e-beam) evaporation system (Beijing Technol Science Co., Ltd., Model TEMD500) was used to coat a layer of material on the surface of the micromotors. Optical videos were taken by a Leica inverted optical microscope (Model DMi8) with a 40× air objective. Fluorescence images of micromotors modified with urease were taken by a confocal laser scanning microscope (CLSM) (Nikon, Model A1). The zeta potential was obtained from Zetasize NANO (Malvern). Two wells connected by a microchannel were manufactured by a 3-D printer (nanoArch P150, BMF Materials Technology Inc., Shenzhen, China). The concentration of exosomes was measured by a Malvern Nanosight NS300. The Raman measurement was carried out on a Horiba LabRAM HR Evolution confocal microscopic Raman spectrometer that was equipped with a 514-nm laser.

Synthesis of Polystyrene (PS) Microparticles. Polystyrene (3 μm) was prepared according to a previous report with some modifications.[27] First, K-30 (0.25 g) was dissolved in a mixture of IPA (45 mL) and deionized water (5 mL). Then styrene (10 g) and AIBN (0.17 g) were added to the previous solution. Subsequently, the mixture was heated to 70 °C and stirred under nitrogen gas flux for 24 h. The obtained polystyrene particles were isolated by centrifugation, washed five times with a mixture of ethanol and deionized (DI) water at the volume ratio of 1:1 and finally dried overnight under vacuum for further use.

The Functionalization of Amine (−NH_2) Inside about Hollow SiO_2 ($HSiO_2$)@Fe@Au ($HSiO_2$FA-NH_2−I). PS particles (50 mg), CTAB (10 mg) and $NH_3.H_2O$ (50 μL) were suspended in a mixture solution containing EtOH (1 mL) and H_2O (1.3 mL) by sonication for 5 min. Then, TEOS (7 μL) and APTES (5 μL) were added to the mixture solution. After this mixture was stirred for 24 h, the PS particles coated with amino-group-decorated silica (PS@SiO_2−NH_2) were collected and washed three times with EtOH. To seal off the amino group on the surface of the silica, another layer of silicon is coated on the surface of PS@SiO_2−NH_2. PS@SiO_2−NH_2 (50 mg), CTAB (10 mg), and $NH_3{\cdot}H_2O$ (50 μL) were suspended in a mixture solution containing EtOH (1 mL) and H_2O (1.3 mL) by sonication for 5 min. Subsequently, only TEOS (7 μL) was added to the mixture solution. After stirred for 24 h, the produced PS particles coated with internal amine-modified silica (PS@SiO_2−NH_2@SiO_2) were collected and washed with EtOH.

The previously prepared PS@SiO_2−NH_2@SiO_2 were suspended in EtOH. Then, 80 μL of ethanol suspension containing PS@SiO_2−NH_2@SiO_2 particles were deposited dropwise onto the glass slide (Φ = 40 mm), which was cleaned by sonication and treated with oxygen plasma for 5 min. A layer of 10 nm Fe and 10 nm Au was then sequentially sputtered onto the PS@SiO_2−NH_2@SiO_2 microspheres using an electron beam (e-beam) evaporation system. The formed PS@SiO_2−NH_2@SiO_2@Fe@Au (PSSFA-NH_2−I) was collected by sonication in DI water and centrifugation. Finally, the PS template was removed by washing with DMF for five times and ethanol for three times. $HSiO_2$@Fe@Au-NH_2−I microparticles ($HSiO_2$FA-NH_2−I) were obtained.

The Functionalization of Amine (−NH_2) Outside Hollow SiO_2 ($HSiO_2$)@Fe@Au ($HSiO_2$FA-NH_2−O). PS particles (50 mg), CTAB (10 mg), and $NH_3{\cdot}H_2O$ (50 μL) were suspended in a mixture solution containing EtOH (1 mL) and H_2O (1.3 mL) by sonication for 5 min. Then, TEOS (7 μL) was added into the mixture solution. After this mixture was stirred for 24 h, the PS particles coated with silica (PS@SiO_2) were collected and washed three times with EtOH. To modify the amino group on the surface of silica, another layer of silicon with an amino group is coated on the surface of PS@SiO_2. PS@SiO_2 (50 mg), CTAB (10 mg) and $NH_3{\cdot}H_2O$ (50 μL) were suspended in a mixture solution containing EtOH (1 mL) and H_2O (1.3 mL) by sonication for 5 min. Subsequently, TEOS (7 μL) and APTES (5 μL) were added into the mixture solution. After stirred for 24 h, the produced PS particles coated with external amine-modified silica (PS@SiO_2@SiO_2−NH_2) were collected and washed with EtOH.

$HSiO_2$@Fe@Au-NH_2−O ($HSiO_2$FA-NH_2−O) microparticles were obtained by using the same protocol described above.

Synthesis of Internal Urease Modified $HSiO_2$FA-NH_2−I ($HSiO_2$FA-Urease-I) and External Urease Modified $HSiO_2$FA-NH_2−O ($HSiO_2$FA-Urease-O). The obtained $HSiO_2$FA-NH_2−I and $HSiO_2$FA-NH_2−O in previous steps were suspended in 1 mL of PBS containing GA (50 μL), respectively. The mixture solution was kept shaking for 3 h. Then, the activated $HSiO_2$FA-NH_2−I and $HSiO_2$FA-NH_2−O were washed five times using PBS and resuspended in 1 mL of PBS containing 5 mg urease. Subsequently, the new mixture solution was shaken for 12 h. Finally, the product was washed five times with DI H_2O.

Optical Video Recording. The movement of the $HSiO_2$FA-Urease-I and $HSiO_2$FA-Urease-O micromotors were observed and

https://doi.org/10.1021/acsnano.3c10405
ACS Nano 2023, 17, 24343−24354

recorded at room temperature by a Leica DMi8 with 40× and 63× objective magnification. The $HSiO_2FA$-Urease-I and $HSiO_2FA$-Urease-O micromotors solution (10 μL) with proper concentration and 10 μL of urea solution with various concentrations (0, 2.5, 5, 10, 25, 50, 100 mM) were placed in a 0.8 mm deep Petri dish and covered with a coverslip to minimize the drifting effect. The movements of the $HSiO_2FA$-Urease-I and $HSiO_2FA$-Urease-O micromotors were recorded by a charge-coupled device (CCD) camera at a frame rate of 20 fps.

The Repulsion Behavior of the Micromotors against Tracer Particles. SiO_2 spheres (400 nm) were selected as tracer particles. Briefly, the aqueous suspension of the $HSiO_2FA$-Urease-I and $HSiO_2FA$-Urease-O micromotors (10 μL) was deposited dropwise onto the Petri dish, followed by adding 10 μL of SiO_2 solution (5 mg/mL) containing urea. The repulsive behaviors between the micromotor and SiO_2 particles were recorded and analyzed.

COMSOL Simulation. A few equations and boundary conditions of the numerical model are worth mentioning. This model was originally developed by Velegol et al.[40] and was recently adapted by Wang et al.[33] for the study of PMMA/AgCl self-diffusiophoretic micromotors.

The distribution of ion concentration was calculated via the *transport of diluted species* module. The active surface of the motor in our model produces ions (NH_4^+ and CO_3^{2-}) at a flux J and consumes the substrate (urea) at a flux of 0.5 J that is proportional to the local substrate concentration. Specifically, J_{urea} [mol/m^2 s] = $(8.12 \times 10^{-8}) \cdot c_{urea} - (1.26 \times 10^{-6})$; this flux equation was obtained by detecting the enzyme catalytic rate at different urea concentrations. Chemicals fluxes due to convention and electromigration were neglected here, because of their relatively small contribution to the overall distribution of ions. The concentrations of each chemicals were calculated based on the following equation at steady state:

$$J_i = -D_i \nabla c_i \tag{1}$$

where J_i, D_i, and c_i are the flux, diffusion coefficient, and concentration of the corresponding chemical i. The starting concentrations c_{0_urea} of urea is set to be 25 mM and 50 mM for $HSiO_2FA$-Urease-I and $HSiO_2FA$-Urease-O micromotors, respectively.

The electrical field and fluid field were calculated via the *electrostatic module* and *creeping flow module*. We assumed the reactions and flows are at steady state and independent of time. Also, we employed the infinitesimal electric double layer (EDL) approximation. The electrical boundary condition at the double layer of the active surface is then set by the normal potential gradients:

$$-\frac{\partial \varphi}{\partial n} = \frac{Jk_B T}{2en_0\left(\frac{1}{D_+} - \frac{1}{D_-}\right)} \tag{2}$$

where φ is the electrical potential, k_B the Boltzmann constant, T the absolute temperature, e the elementary charge, n_0 is the bulk concentration of ions, and D_+ and D_- are the diffusion coefficients of NH_4^+ and CO_3^{2-}, respectively.

The surface electrical boundary condition for the inert surface is $-\frac{\partial \varphi}{\partial n} = 0$, because of no flux. Outside the electrical double layer, the electrostatic problem is defined by the Laplace equation ($\nabla^2 \varphi = 0$). The electrohydrodynamic problem is governed by the Stokes equations:

$$\eta \nabla^2 \mathbf{u} = 0 \tag{3}$$

$$\nabla \cdot \mathbf{u} = 0 \tag{4}$$

where η is the dynamic viscosity of the solution and $\mathbf{u}$ is the flow fluid velocity. The boundaries of the micromotor are set to be electroosmotic with a slip velocity of

$$U = \frac{\zeta_p \varepsilon E'}{\eta} \tag{5}$$

where ζ_p is the zeta potential of the micromotor, ε the medium permittivity, and E' the tangential component of the local electric field.

This numerical model was a two-dimensional axisymmetric model and solved by a finite-element package (COMSOL Multiphysics 6.0). The default parameters in the simulations are set as the following values: $\zeta_p = -50$ mV for the all surface of particles, $D_+ = 1.95 \times 10^{-9}$ m^2/s, and $D_- = 0.92 \times 10^{-9}$ m^2/s. n_0 is 10^{-7} mol/L, as the bulk is neutral solution. The particles are placed in a water-filled simulation block of 500 μm in length and 500 μm in width. The geometry of the micromotors is an open ring (the opening diameter is 0.5 μm) with an outer diameter of 1.6 μm and an inner diameter of 1.5 μm. A scheme of the model can be found in Figure S5 in the Supporting Information.

The Calculated Positions and Speeds of Tracers via the Particle Tracing Module. We assume that the electric field generated by the motor solved above repels the tracer. The velocity of the tracer ball is calculated by Newton's formula:

$$\frac{dmv}{dt} = ES\rho_s \tag{6}$$

where m is the mass of a tracer, v the speed of the tracer, t the time, S the surface area of the tracer ($S = 4\pi R^2$), and ρ_s the surface charge density (which is calculated using the equation $\rho_s = \varepsilon\varphi\kappa$, where ε is the dielectric constant of water at 25 °C, φ is the surface electric potential (approximated here as the zeta potential, ζ_p), and κ the Debye length (~100 nm)). The position r of a tracer can be described by the following equation:

$$r_{i+1} = r_i + v\tau \tag{7}$$

where i is the iteration step and τ is the iteration time step.

Synthesis of $HSiO_2FA$-Urease-I with Aptamers ($HSiO_2FAA$-Urease-I) and $HSiO_2FA$-Urease-O with Aptamers ($HSiO_2FAA$-Urease-O). The thiol-modified CD63 aptamers (5′-CAC CCC ACC TCG CTC CCG TGA CAC TAA TGC TAT TTT TTT TTT TTT TTT-3′-SH, 5 μM) were pretreated with tris(2-carboxyethyl) phosphine hydrochloride (1 mM) overnight. $HSiO_2FA$-Urease-I and $HSiO_2FA$-Urease-O particles were added into the solution containing pretreated aptamers for incubating overnight by Au−S binding, respectively. Then, MCH (1 mM) and BSA (1%) were employed to block the outer Au layer. Finally, $HSiO_2FAA$-Urease-I and $HSiO_2FAA$-Urease-O were washed three times using DI H_2O and suspended in DI H_2O for storage at 4 °C.

Cell Culture and Preparation of Exosomes. Exosomes were isolated from a cell culture medium of human breast cancer (MCF-7). The MCF-7 cells were cultured in DMEM with 10% FBS for 48 h under 37 °C, 5% CO_2 in a humidified incubator. After reaching 80% confluency, the cells were washed with PBS three times and cultured in FBS-free medium for 24 h. Then, the culture medium was collected and centrifuged at 1000g for 5 min to remove the cells and at 16 500g for 20 min to remove large vesicles. The cell debris was removed by filtration using 0.22 μm filters. Then, the exosomes were obtained by ultracentrifuging cell culture medium at 100 000g for 1 h and stored at −80 °C for subsequent experiments.

Capture Efficiency of Exosomes. To test the capture efficiency of exosomes by the $HSiO_2FAA$-Urease-I and $HSiO_2FAA$-Urease-O micromotors, exosomes were suspended in 1 mL of DI water. Various mixtures ($HSiO_2FAA$-Urease-I without urea, $HSiO_2FAA$-Urease-I with urea, $HSiO_2FAA$-Urease-O without urea, $HSiO_2FAA$-Urease-O with urea) were added into the solution of exosomes. After being incubated for 5 min, these micromotors were magnetically separated from the solution. The concentration of exosomes was measured by NTA. The capture efficiency was defined as the ratio of captured exosomes against the total number of exosomes.

Isolation and SERS Sensing of Target Exosomes from Complex Samples. A solution containing $HSiO_2FAA$-Urease-I micromotors and urea was added to the well with the real simulating sample. After the $HSiO_2FAA$-Urease-I micromotors captured the targeted exosomes, these micromotors were magnetically guided across the channel to the clean well. Using the SERS effect of the

https://doi.org/10.1021/acsnano.3c10405
ACS Nano 2023, 17, 24343−24354

coated Au, the Raman signals of exosomes captured by $HSiO_2$FAA-Urease-I micromotors were detected by a confocal Raman spectrometer with a 514-nm laser. For the application of $HSiO_2$FAA-Urease-I micromotors in real samples, we collected human blood and urine samples from a clinic collaboration. To remove cells and sediment, each blood and urine samples were centrifuged at 1000*g* for 20 min at 4 °C and filtered using a 0.22 μm filter membrane. Subsequently, the filtered solution underwent ultrafiltration using a 100 kDa filter unit. Ultimately, the $HSiO_2$FAA-Urease-I micromotors were introduced into the pretreated plasma and urine to investigate their behavior in capturing and detecting exosomes. To evaluate the capture efficiency of the $HSiO_2$FAA-Urease-I micromotors in pretreated plasma and urine, we introduced PKH26 dye to label exosomes with red fluorescence. The alteration in fluorescence intensity within the supernatant was quantified to ascertain the capture efficiency of $HSiO_2$FAA-Urease-I micromotors' capture efficiency.

ASSOCIATED CONTENT

Supporting Information

The Supporting Information is available free of charge at https://pubs.acs.org/doi/10.1021/acsnano.3c10405.

SEM images, TEM images, fluorescence spectrum, zeta potential, geometry of a $HSiO_2$FA-Urease-I and $HSiO_2$FA-Urease-O micromotor, snapshots of the $HSiO_2$FAA-Urease-I micromotor capturing the exosome, the capture efficiency of exosomes using the $HSiO_2$FAA-Urease-I micromotors under different concentrations of urea, analysis of exosome concentration in solution before and after treatment with aptamer-free modified $HSiO_2$FA-Urease-I micromotors measured by NTA, exosome concentrations in the solution after different treatment, urease activity, movement, exosome capture and sensing using the $HSiO_2$FAA-Urease-I micromotor in pretreated urine and plasma are shown in Figures S1−S15. The assignment of SERS signals for the exosomes using the Au coating on the $HSiO_2$FAA-Urease-I micromotors and the comparison between enzymatic micromotors and the other reported exosome isolation approaches based on chemical affinity are shown in Tables S1 and S2 (PDF)

Video S1: Movement of $HSiO_2$FA-Urease-I micromotor in different concentrations of urea solutions. (AVI)

Video S2: Movement of $HSiO_2$FA-Urease-O micromotor in different concentrations of urea solutions (AVI)

Video S3: Influence on surrounding particles from the $HSiO_2$FA-Urease-I and $HSiO_2$FA-Urease-O micromotor (AVI)

Video S4: Exosomes capturing using $HSiO_2$FA-Urease-I micromotor (AVI)

Video S5: Transporting exosome using $HSiO_2$FA-Urease-I micromotor (AVI)

Video S6: Movement of $HSiO_2$FA-Urease-I micromotor with exosome from the capture well to the detection well under a magnetic field (AVI)

Video S7: Movement of $HSiO_2$FA-Urease-I micromotor in pretreated plasma and urine solution containing 25 mM urea (AVI)

AUTHOR INFORMATION

Corresponding Authors

Wenjun Chen − *School of Materials Science and Engineering, Harbin Institute of Technology (Shenzhen), Guangdong, Shenzhen 518055, China; Sauvage Laboratory for Smart Materials, Harbin Institute of Technology (Shenzhen), Guangdong, Shenzhen 518055, China;* orcid.org/0000-0001-7282-199X; Email: wenjun.chen0521@gmail.com

Wei Wang − *School of Materials Science and Engineering, Harbin Institute of Technology (Shenzhen), Guangdong, Shenzhen 518055, China*; Email: weiwangsz@hit.edu.cn

Xing Ma − *School of Materials Science and Engineering, Harbin Institute of Technology (Shenzhen), Guangdong, Shenzhen 518055, China; Sauvage Laboratory for Smart Materials, Harbin Institute of Technology (Shenzhen), Guangdong, Shenzhen 518055, China;* orcid.org/0000-0002-2248-4806; Email: maxing@hit.edu.cn

Authors

Xiaoxia Liu − *School of Materials Science and Engineering, Harbin Institute of Technology (Shenzhen), Guangdong, Shenzhen 518055, China; Sauvage Laboratory for Smart Materials, Harbin Institute of Technology (Shenzhen), Guangdong, Shenzhen 518055, China*

Yong Wang − *Key Laboratory of Clinical Laboratory Diagnostics (Ministry of Education), College of Laboratory Medicine, Chongqing Medical University, Chongqing 400016, China*

Yixin Peng − *School of Materials Science and Engineering, Harbin Institute of Technology (Shenzhen), Guangdong, Shenzhen 518055, China*

Jinjin Shi − *School of Pharmaceutical Sciences, Zhengzhou University, Zhengzhou 450001, China;* orcid.org/0000-0003-1531-7265

Complete contact information is available at: https://pubs.acs.org/10.1021/acsnano.3c10405

Author Contributions

X. Liu and X. Ma conceived and designed the experiments. X. Liu conducted most of the experiments. Y. Wang was responsible for video recording of the micromotors and data analysis. Y. Peng simulated the flow field and the electric field around the micromotors. J. Shi provided the exosomes. W. Chen, W. Wang, and X. Ma revised the manuscript.

Funding

National Natural Science Foundation of China (Nos. 52072095, 52202347, T2322006), Shenzhen Science and Technology Program (Nos. KQTD20170809110344233, RCBS20210609103646022, RCYX20210609103122038), Guangdong Basic and Applied Basic Research Foundation (No. 2021A1515110272), and Natural Science Foundation of Chongqing, China (No. 2023NSCQ-MSX1158).

Notes

The authors declare no competing financial interest.

ACKNOWLEDGMENTS

The authors thank the financial support from National Natural Science Foundation of China (Nos. 52072095, 52202347, T2322006), Shenzhen Science and Technology Program (Nos. KQTD20170809110344233, RCBS20210609103646022, RCYX20210609103122038), Guangdong Basic and Applied Basic Research Foundation (No. 2021A1515110272), and Natural Science Foundation of Chongqing, China (No. 2023NSCQ-MSX1158).

REFERENCES

(1) Feng, Y.; An, M.; Liu, Y.; Sarwar, M. T.; Yang, H. Advances in Chemically Powered Micro/Nanorobots for Biological Applications: A Review. *Adv. Funct. Mater.* **2023**, *33*, No. 2209883.

(2) Sanchez, S.; Soler, L.; Katuri, J. Chemically Powered Micro- and Nanomotors. *Angew. Chem., Int. Ed.* **2015**, *54* (5), 1414−1444.

(3) Arque, X.; Patino, T.; Sanchez, S. Enzyme-Powered Micro- and Nano-motors: Key Parameters for an Application-Oriented Design. *Chem. Sci.* **2022**, *13* (32), 9128−9146.

(4) Zhao, X.; Gentile, K.; Mohajerani, F.; Sen, A. Powering Motion with Enzymes. *Acc. Chem. Res.* **2018**, *51* (10), 2373−2381.

(5) Yang, Y.; Arque, X.; Patino, T.; Guillerm, V.; Blersch, P.-R.; Perez-Carvajal, J.; Imaz, I.; Maspoch, D.; Sanchez, S. Enzyme-Powered Porous Micromotors Built from a Hierarchical Micro- and Mesoporous UiO-Type Metal-Organic Framework. *J. Am. Chem. Soc.* **2020**, *142* (50), 20962−20967.

(6) Orozco, J.; Garcia-Gradilla, V.; D'Agostino, M.; Gao, W.; Cortes, A.; Wang, J. Artificial Enzyme-Powered Microfish for Water-Quality Testing. *ACS Nano* **2013**, *7* (1), 818−824.

(7) Ma, X.; Wang, X.; Hahn, K.; Sanchez, S. Motion Control of Urea-Powered Biocompatible Hollow Microcapsules. *ACS Nano* **2016**, *10* (3), 3597−3605.

(8) Hortelao, A. C.; Simo, C.; Guix, M.; Guallar-Garrido, S.; Julian, E.; Vilela, D.; Rejc, L.; Ramos-Cabrer, P.; Cossio, U.; Gomez-Vallejo, V.; et al. Swarming Behavior and In Vivo Monitoring of Enzymatic Nanomotors within the Bladder. *Sci. Robot.* **2021**, *6* (52), No. eabd2823.

(9) Liu, M.; Chen, L.; Zhao, Z.; Liu, M.; Zhao, T.; Ma, Y.; Zhou, Q.; Ibrahim, Y. S.; Elzatahry, A. A.; Li, X.; Zhao, D. Enzyme-Based Mesoporous Nanomotors with Near-Infrared Optical Brakes. *J. Am. Chem. Soc.* **2022**, *144* (9), 3892−3901.

(10) Zhang, B.; Pan, H.; Chen, Z.; Yin, T.; Zheng, M.; Cai, L. Twin-Bioengine Self-Adaptive Micro/Nanorobots Using Enzyme Actuation and Macrophage Relay for Gastrointestinal Inflammation Therapy. *Sci. Adv.* **2023**, *9* (8), No. eadc8978.

(11) Wang, L.; Hortelao, A. C.; Huang, X.; Sanchez, S. Lipase-Powered Mesoporous Silica Nanomotors for Triglyceride Degradation. *Angew. Chem., Int. Ed.* **2019**, *58* (24), 7992−7996.

(12) Wang, L.; Marciello, M.; Estevez-Gay, M.; Soto Rodriguez, P. E. D.; Luengo Morato, Y.; Iglesias-Fernandez, J.; Huang, X.; Osuna, S.; Filice, M.; Sanchez, S. Enzyme Conformation Influences the Performance of Lipase-powered Nanomotors. *Angew. Chem., Int. Ed.* **2020**, *59* (47), 21080−21087.

(13) Hortelao, A. C.; Carrascosa, R.; Murillo-Cremaes, N.; Patino, T.; Sanchez, S. Targeting 3D Bladder Cancer Spheroids with Urease-Powered Nanomotors. *ACS Nano* **2019**, *13* (1), 429−439.

(14) Zhao, L.; Liu, Y.; Xie, S.; Ran, P.; Wei, J.; Liu, Q.; Li, X. Janus Micromotors for Motion-Capture-Ratiometric Fluorescence Detection of Circulating Tumor Cells. *Chem. Eng. J.* **2020**, *382*, No. 123041.

(15) Skog, J.; Wurdinger, T.; van Rijn, S.; Meijer, D. H.; Gainche, L.; Curry, W. T.; Carter, B. S.; Krichevsky, A. M.; Breakefield, X. O. Glioblastoma Microvesicles Transport RNA and Proteins that Promote Tumour Growth and Provide Diagnostic Biomarkers. *Nat. Cell Biol.* **2008**, *10* (12), 1470−1476.

(16) Anastasiadou, E.; Slack, F. J. Malicious Exosomes. *Science* **2014**, *346* (6216), 1459−1460.

(17) Doyle, L. M.; Wang, M. Z. Overview of Extracellular Vesicles, Their Origin, Composition, Purpose, and Methods for Exosome Isolation and Analysis. *Cells* **2019**, *8* (7), 727.

(18) Caradec, J.; Kharmate, G.; Hosseini-Beheshti, E.; Adomat, H.; Gleave, M.; Guns, E. Reproducibility and Efficiency of Serum-Derived Exosome Extraction Methods. *Clin. Biochem.* **2014**, *47* (13), 1286−1292.

(19) Lozano-Ramos, I.; Bancu, I.; Oliveira-Tercero, A.; Pilar Armengol, M.; Menezes-Neto, A.; Del Portillo, H. A.; Lauzurica-Valdemoros, R.; Borras, F. E. Size-Exclusion Chromatography-Based Enrichment of Extracellular Vesicles from Urine Samples. *J. Extracell. Vesicles* **2015**, *4*, 20.

(20) Mincheva-Nilsson, L.; Baranov, V.; Nagaeva, O.; Dehlin, E. Isolation and Characterization of Exosomes from Cultures of Tissue Explants and Cell Lines. *Curr. Protoc. Immunol.* **2016**, *115*, 144211−144221.

(21) Manri, C.; Yokoi, T.; Nishida, H. Size-Selective Harvesting of Extracellular Vesicles for Strategic Analyses Towards Tumor Diagnoses. *Appl. Biochem. Biotechnol.* **2017**, *182* (2), 609−623.

(22) Wan, Y.; Cheng, G.; Liu, X.; Hao, S.-J.; Nisic, M.; Zhu, C.-D.; Xia, Y.-Q.; Li, W.-Q.; Wang, Z.-G.; Zhang, W.-L.; et al. Rapid Magnetic Isolation of Extracellular Vesicles Via Lipid-Based Nanoprobes. *Nat. Biomed. Eng.* **2017**, *1* (4), 0058.

(23) Jiang, Y.; Shi, M.; Liu, Y.; Wan, S.; Cui, C.; Zhang, L.; Tan, W. Aptamer/AuNP Biosensor for Colorimetric Profiling of Exosomal Proteins. *Angew. Chem., Int. Ed.* **2017**, *56* (39), 11916−11920.

(24) Wu, L.; Wang, Y.; Xu, X.; Liu, Y.; Lin, B.; Zhang, M.; Zhang, J.; Wan, S.; Yang, C.; Tan, W. Aptamer-Based Detection of Circulating Targets for Precision Medicine. *Chem. Rev.* **2021**, *121* (19), 12035−12105.

(25) Xiong, K.; Lin, J.; Chen, Q.; Gao, T.; Xu, L.; Guan, J. An Axis-asymmetric Self-driven Micromotor That Can Perform Precession Multiplying "On-the-Fly" Mass Transfer. *Matter* **2023**, *6* (3), 907−924.

(26) Lin, J.; Xiong, K.; Hu, J.; Li, Z.; Xu, L.; Guan, J. Micromotors with Spontaneous Multipattern Motion and Microvortex for Enhanced "On-the-Fly" Molecule Enrichment. *Adv. Intell. Syst.* **2023**, *5*, 2300386.

(27) Xu, D.; Zhou, C.; Zhan, C.; Wang, Y.; You, Y.; Pan, X.; Jiao, J.; Zhang, R.; Dong, Z.; Wang, W.; Ma, X. Enzymatic Micromotors as a Mobile Photosensitizer Platform for Highly Efficient On-Chip Targeted Antibacteria Photodynamic Therapy. *Adv. Funct. Mater.* **2019**, *29* (17), No. 1807727.

(28) Ma, X.; Wang, X.; Hahn, K.; Sánchez, S. Motion Control of Urea-Powered Biocompatible Hollow Microcapsules. *ACS Nano* **2016**, *10* (3), 3597−3605.

(29) Tsai, H.-C.; Doong, R.-A. Preparation and Characterization of Urease-Encapsulated Biosensors in Poly(vinyl alcohol)-Modified Silica Sol-Gel Materials. *Biosens. Bioelectron* **2007**, *23* (1), 66−73.

(30) Kistiakowsky, G. B.; Rosenberg, A. J. The Kinetics of Urea Hydrolysis by Urease1. *J. Am. Chem. Soc.* **1952**, *74* (20), 5020−5025.

(31) Park, H.; Jung, Y. M.; You, J. K.; Hong, W. H.; Kim, J.-N. Analysis of the CO_2 and NH_3 Reaction in an Aqueous Solution by 2D IR COS: Formation of Bicarbonate and Carbamate. *J. Phys. Chem. A* **2008**, *112* (29), 6558−6562.

(32) Feng, Y.; Yuan, Y.; Wan, J.; Yang, C.; Hao, X.; Gao, Z.; Luo, M.; Guan, J. Self-Adaptive Enzyme-Powered Micromotors with Switchable Propulsion Mechanism and Motion Directionality. *Appl. Phys. Rev.* **2021**, *8* (1), No. 011406.

(33) Zhou, C.; Zhang, H. P.; Tang, J.; Wang, W. Photochemically Powered AgCl Janus Micromotors as a Model System to Understand Ionic Self-Diffusiophoresis. *Langmuir* **2018**, *34* (10), 3289−3295.

(34) Ding, S.-Y.; You, E.-M.; Tian, Z.-Q.; Moskovits, M. Electromagnetic Theories of Surface-Enhanced Raman Spectroscopy. *Chem. Soc. Rev.* **2017**, *46* (13), 4042−4076.

(35) Fraire, J. C.; Stremersch, S.; Bouckaert, D.; Monteyne, T.; De Beer, T.; Wuytens, P.; De Rycke, R.; Skirtach, A. G.; Raemdonck, K.; De Smedt, S.; Braeckmans, K.; et al. Improved Label-Free Identification of Individual Exosome-like Vesicles with Au@Ag Nanoparticles as SERS Substrate. *ACS Appl. Mater. Interfaces* **2019**, *11* (43), 39424−39435.

(36) Yan, Z.; Dutta, S.; Liu, Z.; Yu, X.; Mesgarzadeh, N.; Ji, F.; Bitan, G.; Xie, Y.-H. A Label-Free Platform for Identification of Exosomes from Different Sources. *ACS Sens.* **2019**, *4* (2), 488−497.

(37) Hao, N.; Liu, P.; Bachman, H.; Pei, Z.; Zhang, P.; Rufo, J.; Wang, Z.; Zhao, S.; Huang, T. J. Acoustofluidics-Assisted Engineering of Multifunctional Three-Dimensional Zinc Oxide Nanoarrays. *ACS Nano* **2020**, *14* (5), 6150−6163.

(38) Zhan, X.; Wang, J.; Xiong, Z.; Zhang, X.; Zhou, Y.; Zheng, J.; Chen, J.; Feng, S.-P.; Tang, J. Enhanced Ion Tolerance of

https://doi.org/10.1021/acsnano.3c10405
ACS Nano 2023, 17, 24343−24354

Electrokinetic Locomotion in Polyelectrolyte-Coated Microswimmer. *Nat. Commun.* **2019**, *10* (1), 3921.
(39) Sridhar, V.; Podjaski, F.; Alapan, Y.; Kröger, J.; Grunenberg, L.; Kishore, V.; Lotsch, B. V.; Sitti, M. Light-Driven Carbon Nitride Microswimmers with Propulsion in Biological and Ionic Media and Responsive On-Demand Drug Delivery. *Sci. Robot.* **2022**, *7* (62), No. eabm1421.
(40) Chiang, T.-Y.; Velegol, D. Localized Electroosmosis (LEO) Induced by Spherical Colloidal Motors. *Langmuir* **2014**, *30* (10), 2600−2607.

https://doi.org/10.1021/acsnano.3c10405
ACS Nano 2023, 17, 24343−24354